Title

Sample preparation free tissue imaging using Laser Desorption – Rapid Evaporative Ionisation Mass spectrometry (LD-REIMS)

Authors

Daniel Simon[1,2], Gabriel Stefan Horkovics-Kovats[3,4], Yuchen Xiang[1], Julia Abda[1], Dimitris Papanastasiou[5], Hui-Yu Ho[1,6], Haixing Wang[1], Richard Schäffer[3], Tamas Karancsi[3], Anna Mroz[1], Laurine Lagache[7], Julia Balog[3], Isabelle Fournier[7], Josephine Bunch[8], Zoltan Takats[1,2*]

Affiliations

1 Department of Metabolism, Digestion and Reproduction, Imperial College London, London, United Kingdom

2 Rosalind Franklin Institute, Harwell, United Kingdom

3 Waters Research Center, Budapest, Hungary

4 Hevesy György Doctoral School of Chemistry, Eötvös Loránd University, Budapest, Hungary

5 Fasmatech, Athens, Greece

6 Department of General Surgery, Chang Gung Memorial Hospital, Linkou, Chang Gung University, Taoyuan, Taiwan

7 PRISM Inserm U1192, University of Lille, Lille, France

8 National Physical Laboratory, London, United Kingdom

Abstract

Laser desorption ionisation (LDI) is generally considered to be an inferior ionisation modality to matrix assisted LDI (MALDI), providing information solely on lipids with low sensitivity. The

current study demonstrates that the combination of ambient LDI with in-source surface-induced declustering provides sensitivity and chemical coverage comparable to MALDI. The setup was characterised for infrared laser desorption using two different laser systems and was successfully used for ambient mass spectrometric imaging. 20 µm spatial resolution was achieved with oversampling, approaching single-cell resolution, while metabolites and lipids ranging from amino acids through carbohydrates and nuclear bases to complex glycolipids were successfully detected. The technique was also tested as a platform for MS-guided surgery, raising the possibility of using a single technique for generating histological and in-vivo data. The results suggest that the new method can form the basis for a new histological classification system for surgery and pathology environments closing this 150 year old diagnostic gap.

Teaser

A new mass spectrometric imaging method bridging histopathology and in-vivo interventional tissue identification methodology.

Introduction

Laser desorption ionisation (LDI) mass spectrometry was among the first analytical applications using lasers in the late 1960s (*1, 2*). As one of the first techniques with the aim to analyse biomolecules, laser desorption ionization (LDI) was introduced in the 1960s; also for imaging the laser microprobe mass analysis (LAMMA) technique which was introduced in the 1970s (*3*). While the rationale of this application for tissue analysis is straightforward, LDI has never gained true popularity as an organic MS method due to a handful of inherent problems stemming from the fundamentals of biological matter-laser interactions. These problems include (1) thermally induced condensation reactions which turn biological samples into a three-dimensional, highly cross-linked polymer structure (eventually leading to carbonisation) efficiently trapping analyte molecules, (2) formation of a large amount of neutral molecules in the gas phase relative to the formation of ions (3) aerosolization of samples leading to particles containing up to 10^8 – 10^9

molecules (*4–6*). All these three effects act against ionisation efficiency, deeming the approach insensitive for most bioanalytical applications. The first significant breakthrough regarding solving these problems was the development of matrix assisted LDI (MALDI), where soluble analytes are extracted into a crystalline layer of small organic molecules termed as 'matrix' (*7*). The basic requirements for a matrix include high absorbance at the wavelength of the laser and the formation of only gaseous degradation products on laser irradiation (*8*). The MALDI sample preparation process transfers soluble analytes into an environment close to ideal for laser desorption, giving several orders of magnitude improvement on the ionisation efficiency of small molecules (metabolites, lipids) and allowing the ionisation of macromolecular species like intact proteins. Nevertheless, MALDI predominantly tackles problem 1 (see above) as it still produces a high amount of neutrals and clusters while introducing a set of new problems revolving mainly around the deposition of the matrix layer (*9*). Following the development of MALDI, a number of different approaches have been tested for tackling problem 2 (formation of gas-phase neutrals), either in combination with matrix assistance or without it. These methods, collectively termed 'post desorption ionisation' or shortly just 'post-ionisation' methods, ranged from photoionization to discharge ionisation approaches used in conjunction with LDI. One of the most sophisticated ones, MALDI-2, revolutionised MALDI applications in course of the last five years by further improving the sensitivity of the technique by 2-3 orders of magnitude (*10*). We also demonstrated recently that a low-temperature plasma post-ionisation results in similar sensitivity improvement even in the absence of matrix (*11, 12*). However, none of these approaches provided a reasonable solution for problem #3, the formation of large molecular clusters resistant to post-ionisation techniques or the heating of certain parts of the ion path (e.g. atmospheric interface in case of AP-MALDI where the cluster formation is particularly profound due to the limited expansion of desorption plume under high-pressure conditions). The problem of cluster formation is not limited to LDI; practically all methods developed for the ionisation of condensed phase samples suffer

from this phenomenon, including electrospray, the single most widely used ionisation method (*13, 14*). The idea of utilizing surface-induced dissociation to tackle this problem originated from the electrospray droplet impact technique, an approach developed for enhancing the ionisation efficiency of electrospray ionisation (*15*). Clusters accelerated by the adiabatic expansion following the first gas conductance limit in an atmospheric interface can be impacted against a solid target to induce their dissociation in a straightforward manner. Advantages of the approach include the short timescale compared to slow heating methods and the independence of cluster size compared to gas collision methods. As it is discussed below, the method works in practice and fulfils the expectations outlined above.

Atmospheric pressure laser desorption ionisation methods – despite the poor sensitivity – have gained momentum following our initial publication on the utilisation of a number of different laser systems for direct tissue analysis (*16*). The subsequently developed Spider Mass system utilising resonant IR laser at 3 μm as well as the CO_2 laser system were successfully used for bulk tissue analysis with a clear perspective for direct surgical utilisation, especially in the case of surgical lasers (*17*). Further noteworthy development was the use of picosecond infrared lasers for the same purpose resulting in clear surgical advantages, including minimal thermal spread and ultrafine dissection (*18*). The current project was driven by the motivation of developing a system which is equally capable of supporting mass spectrometry-guided surgical interventions and molecular histopathology. Although tissue identification has been critically important in both surgery and pathology, the in-situ decision making in surgery has almost always been based on sensory information (colour, physical consistency) in contrast to histopathology, where tissue classification is based on cellular morphology. Consequently, the ‘macroscopic’ tumour margin in the case of cancer surgery may be significantly different from the ‘microscopic’ one, potentially resulting in incomplete tumour resections. Developing a technology equally capable of histological imaging with a view of co-registering the resulting data with classical histopathology

and collecting in-situ, in-vivo data would eventually close this gap and enable surgeons to operate with histological precision.

Results

LD-REIMS setup development

A multipurpose LD-REIMS platform was constructed to perform LD-REIMS tissue imaging experiments (see **Figure 1A)**. The setup consists of a laser source, a delivery system of the laser beam (open beam guided with mirrors in case of OPO, optical fibre waveguide in case of CO_2) and focal optics, where the final focusing is performed using a 20 mm focal distance lens. The imaging setup and focal optics for the CO_2 laser are fundamentally identical. After carefully optimising the system, the best focal spot sizes achieved with the OPO laser were approximately 60 µm and 70 µm for the CO_2 laser; improving the optical performances (by using shorter focal distance lenses with suitable aberration correction, e.g. aspherical lenses) might allow further reduction in focal spot sizes. At the measured spot sizes, the laser power density for both lasers was around 1 kW/cm^2 (5 J/cm^2 fluence in the case of the pulsed OPO laser). Due to the pulsed operation mode of the OPO laser and the maximum 20 Hz pulse frequency, the sampling frequency of the mass spectrometer can only be set to a value which is dividable by 20. The imaging speed was set to 10 pixels/second as a good compromise between sensitivity and speed. The laser ablation/ionisation setup was coupled with a metal capillary atmospheric interface custom-built for the purpose of this study. The interface (**figure 1B**) incorporated a matrix introduction element, and it was prepared to accommodate the impact target used for declustering.

Implementation of surface-induced desclustering in the atmospheric interface:

Our primary objective was to achieve sensitivity and robustness that is suitable for routine tissue profiling applications. Alternatively to previous laser desorption ionisation setups, we employed a heated impactor element in the vacuum interface, which enhances ion formation by facilitating the declustering of the sample aerosol particles. The fundamental questions regarding this

instrumental setup were whether the particles accelerated by the free jet expansion would have sufficient velocity to dissociate and whether the ion optics of the mass spectrometer could capture ionic species formed on the impact event. Further questions were raised on the energetics of the process. To simulate the impact phenomenon of the cluster on the impactor surface, a series of numerical simulations were conducted to design and characterise the optimal impactor surface (**Figure 2A-O**).

The primary particle trajectory simulations revealed that the majority of particles entering the intermediate vacuum regime of the mass spectrometer impact into the jet disruptor surface at an average impact velocity of approximately 600 m/s. The specific kinetic energy of the particles (100 kDa, 10.2 nm diameter) is actually very low – it is ~ 2 eV/kDa, insufficient to break covalent bonds, but certainly sufficient to break up molecular clusters. The trajectory simulations for secondary particles (shown on **Figure 2V**) clearly showed that even individual molecular ions of complex lipids (represented by 1kDa) particles are readily entering the travelling wave ring electrode ion conduit.

In line with the expectations, presence of a spherical collision surface in the free-jet flow region enhanced the signal significantly as it is demonstrated by **Figure 2V**. The optimum distance between the capillary inlet and the surface was experimentally determined (based on obtained signal intensity) to be 5 mm. The results of the simulations also show that optimal ion yields can be achieved with a 3 mm diameter spherical collision surface positioned 5 mm from the MS transfer capillary. This geometric setup allows the free jet expansion and acceleration of the sample droplets, which collide with the optimally located impactor surface for maximum ionisation efficiency. The optimal distance shows a good correlation with the position of the Mach-disk region of the free jet. The velocity and the kinetic energy of the individual particles is the maximum before the Mach-disk, thus the positioning of the impactor surface at this region explains the highest ion yields obtained by the high velocity impact at the surface. Although the

introduction of a solid collision target resulted in a dramatic improvement of signal intensity, the time-dependent signal intensity in this case also showed a remarkable decline on the timescale of minutes. We were able to recover full signal intensity by thoroughly cleaning the surface, however regular cleaning after few 10 minutes of use was deemed to be incompatible with the envisioned biomedical applications. In order to overcome this problem, a surface with controlled temperature in the range of ambient to ~ 1400K was implemented by using a Kanthal D coil. Although the coil (or band) does not provide a well-characterised surface geometry, any coating (e.g. a ceramic tube) results in significant drop in the temperature of the surface at the collision point due to the cooling effect of the free jet expansion. Experiments show that heating the surface of the impactor to around 1200K dramatically increase signal intensity and decrease memory/carry over issues. Besides providing stable signal for several hours, the introduction of heated surface increased the signal intensity by further three orders of magnitude (**Supporting Figure 1**) compared to the cold surface. The elevated temperature of the collision surface enhances the declustering and provide additional thermal energy to complete the subsequent desolvation process to yield individual molecular ions for analysis in the mass spectrometer. The elimination of memory effects and increase in sensitivity allowed us to utilize the laser desorption method for imaging experiments which require instrument stability over extended periods of measurement time.

Laser parameter optimisation:

The laser ablation process producing primary aerosol is expected to be sensitive to the laser parameters including wavelength and fluence among others. Several groups published the successful application of different infrared lasers for tissue ablation and these lasers are commercially available for medical tissue manipulation. However, the mechanism of the ablation process remains poorly understood with the exception of MALDI applications (*19–21*). We have tested two laser systems including a surgical CO_2 laser emitting at 10600 nm and a mid-infrared

Optical Parametric oscillator (OPO) (tuneable between 2700 – 3100 nm) laser, both coupled with a handheld sampling device for human breast tumour tissue analysis. With the shorter pulse width (5 ns vs. 100 µs) OPO laser the optimised spectral quality (Signal-to-noise ratio and signal intensity) was found to be better in the complex lipid region (600 – 1000 m/z) (**Figure 3 A-D**) which has been widely used to establish histological classification (*22*). Univariate analysis of the dataset also confirms the previous assessment, a number of significant features observed were larger (286 in case of CO_2 laser and 1082 in case of OPO laser) using the OPO laser system (**Figure 3 E-F**). Visualising individual significant metabolic and lipidomic species (**Figure 3 G-K**) also confirms this, as the same features observed with both lasers show a clearer distribution using the OPO laser compared to the CO2 laser. The two main differences between these laser systems are the output wavelength and pulse width. The differences observed were associated with the different levels of thermal confinement, which is a phenomenon observed when laser pulses interact with solid surfaces (*23*). Short (5 -7 nanoseconds in the current case) laser pulses cause negligible thermal degradation of the biological material because most of the laser energy is utilised for the cavitation-induced ablation/explosion, while in the case of longer pulse width (0.1 milliseconds in the current case) laser, the irradiation extends well beyond the explosion, even inducing thermal degradation of molecular species. Slow thermal degradation of biological macromolecules generally involves condensation reactions via loss of water and ammonia from hydroxyl and amino moieties (cf. Mallard reaction) yielding a cross-linked covalent matrix eventually turning into amorphous carbon (carbonisation) (*24*). This process effectively shifts the aerosol formation from aqueous droplets towards soot. The downstream declustering process is only effective for liquid droplets as the energy regime is not sufficient to break up the covalent matrix of soot/carbon particles, resulting in poor sensitivity. Based on these findings, further experiments with even shorter (picosecond – femtosecond) pulsed lasers are planned. Picosecond laser pulse widths would allow the ablation to be fully in the stress-confined regime, increasing

the efficiency of ablating intact biomolecules (*25*). The effects of wavelength were also tested with the tuneable OPO laser in the available wavelength range using pork liver samples. From the data, four mass bins, 279.25, 303.25, 766.55 and 885.55 (associated with the deprotonated negative ion of linoleic acid, arachidonic acid, phosphatidylethanolamine PE (38:4) and phosphatidylinositol PI (38:4) respectively) were selected for the analysis of laser wavelength, shown on **fig. 4 A-D.** The results show that there is an optimal wavelength between 2950 – 3000 nm for intensities of important molecular species, which wavelength range falls close to the wavelength of 2940 nm, which is the O-H bond stretch absorption maximum wavelength. To characterise the spectral pattern-level changes associated with different wavelengths, multivariate statistical analysis (Principal Component Analysis - PCA) was performed on the obtained data. The PCA plot (**supporting fig. 2**) shows no significant separation or differences among data points except from the data obtained at 2750 nm. Looking closer at the data, the signal-to-noise ratio for the 2750 nm measurement point was significantly lower than at any other wavelength, resulting in the separation from the rest of the group. These results suggest that the laser interaction with the tissue is limited to the desorption/mobilization due to the rapid heating of endogenous water and there are no additional interactions (e.g. photochemical ionisation) between the laser radiation and the sampled material. These results fall in line with results obtained by other groups that also utilise endogenous water content to ablate tissues using laser desorption (*25*, *26*).

The effect of laser fluence was tested by using different focal optic lenses and the laser operated at different power levels. Ø1 ZnSe aspheric lenses (f = 12.7 mm; f = 25 mm), Ø1/2 CaF_2 plano-convex 20 mm and f = 6 mm) lenses were used to test the ablation characteristics at different laser fluences using pork liver tissues, the tested parameters can be found in **table 1.** The best SNR was achieved with the highest laser fluence using the shorter focal ZnSe lens (at 6.02 J/cm^2), and a characteristic ammonia loss (previously observed with REIMS technique) (*24*) was observed

within the phospholipid region in the spectra, specifically in case of the phosphatidylethanolamine (PE) species. The ratio of observed $[M\text{-}NH_4]^-$ to $[M\text{-}H]^-$ gradually shifted towards a more prominent ammonia loss for PE molecules, as can be seen in **figure 4 E-F.** A PCA model was also generated using this dataset, where the most prominent differentiating factor in PC1 was observed to be the ammonia loss detailed above. Significant separation was observed in spectra obtained between fluence above and below 4.47 J/cm^2 which separation is primarily driven by the effects explained above. The loading and the 3D PC models are shown in **figure 4 G-H**. Higher energy ablation caused a more stable and reproducible ammonia loss effect, which improved the reproducibility and robustness of the technique overall. Based on these results the minimal ablation threshold for LD-REIMS reproducible data was determined to be at 4.50 J/cm^2, and the laser fluence of 5 J/cm^2 was chosen for the imaging experiments below.

Imaging mass spectrometry

Mouse brain mass spectral images were acquired using both lasers at 70 µm raster size, the results of the imaging are shown on **supporting figure 3** (for the OPO laser) and **supporting figure 4** (for the CO_2 laser). The data reveals that both methods are capable of acquiring information from spatially heterogeneous samples, however, the imaging data obtained with the OPO laser had better sensitivity and SNR ratios, which was expected due to the previously mentioned physical differences between the different lasers. The spectral profile mainly consists of small molecules (metabolites, fatty acids and phospholipids), which falls in line with results obtained during previous iKnife experiments. A list of tentatively identified molecules is given in **table 2.** The annotation was performed using accurate mass analysis and using the Chemical Abstract Services database. The set of observed molecular species show good overlap with species described by previous literature on applied laser desorption or REIMS-based MS techniques (*27*).

To challenge the resolution limit of the experiment, the concept of oversampling imaging was tested using the OPO laser with the LD-REIMS imaging setup. At current spot sizes (60 µm)

different imaging raster sizes were tested on coronal mouse brain tissue sections to determine the maximum achievable resolution. The improvement of the spatial resolution of MSI techniques is one of the main objectives of the field. To achieve this, several different approaches have been described in the literature. Oversampling using the analytical beam has been proposed and successfully demonstrated using MALDI technique (*28, 29*). Other approaches use post-ionisation steps like MALDI-2 after sampling to achieve sub-micron imaging resolution (*10*). Using the oversampling approach with the OPO laser setup, different raster size images were acquired at 70, 50, 30 and 20 µm pixel size (see **supporting figure 2**). Using the molecular ion of adenine ($[M-H]^-$ 134.034 m/z) the fine structure of the hippocampal region was identified on the images. As the pixel size decreases, the details of the dentate gyrus region become better defined, and the contrast between the polymorph and the granule cell layer increases. At 30 µm or smaller raster sizes, the fine structures of the stratum radiatum and stratum lacunosum-moleculare regions in the mouse brain become observable as well. The currently achieved 20 µm resolution limit makes the LD-REIMS technique a competitive technique with other MSI techniques. With further planned optimisation, the current imaging setup could acquire images with single-cell resolution. The higher-resolution images provide superior imaging data; however, this comes at the price of significantly increased analysis time. The imaging experiment of a coronal mouse brain section at 70 µm took 40 minutes using 10 pixel/second acquisition rate, and a similar-sized tissue section analysed at 20 µm using the same speed requires more than six hours.

Clinical application of mass spectral imaging

A clinical case study was performed with both laser setups using cancerous human breast tissue samples. Human breast tumour samples were chosen to demonstrate the molecular pathology capabilities of the system. 12 µm thick breast tumour sections were mounted on standard glass slides and imaged using the prototype imaging setup with both lasers without any additional sample preparation steps. The data obtained from the imaging experiments were compared with

the gold standard Hematoxylin-Eosin staining method, the results are shown on **Figure 5** evaluated using hyperspectral correlation methods (*30*). The characteristic differences in molecular profiles found in the imaging data show good correlation with the histologically separated tissue regions that differentiate cancerous and healthy tissue regions. Comparing data from the different lasers, the OPO laser operated at 2940 nm was found to be superior, which observation falls in line with expectations.

The main detected class of molecules are glycerophospholipids and triglycerides (mainly cell membrane compounds), additionally several fatty acids, small molecules and metabolites were observed as well, which may provide valuable insight on clinically important questions, such as differentiating between breast fibroadenoma and cancer tissues.

LD-REIMS is a powerful technology for sample preparation free, untargeted tissue imaging, suitable for label free molecular histopathology, and has the potential to be an efficient tool in pathology and drug discovery laboratories around the world. Beyond these advantages the technology also bridges imaging MS with in-vivo MS. The REIMS based intelligent surgical device (iKnife) technology has been demonstrated for *in vivo* tissue characterisation, however the technique is strongly dependent on the underlying classification models (*31–33*). To perform any tissue classification, a histologically validated database is required to provide adequate references for accurate diagnosis. The required data is usually produced by analyzing excised tissue specimens using the surgical energy device, where bulk tissue is ablated and the resulting aerosol is analyzed by means of REIMS. The remaining tissue is sent for histological assessment to determine pathological status of the ablated cells. This process however carries a certain degree of uncertainty since the ablation is performed using a handheld probe, which causes significant variance in the ablated tissue volume that can lead to sampling a mixture of cells belonging to different histological classes. The pathologist also provides an assessment not based on the ablated tissue, but on the margin remaining after the ablation process which brings another level

of uncertainty to the database, as the exact histological composition of the ablated tissues cannot be properly determined. Since LD-REIMS imaging and the iKnife uses the same mass spectrometric experimental setup, translating the data from tissue sections to bulk *in vivo* tissue analysis should be feasible. As the laser can give better spatial resolution than the diathermy and therefore a lower chance of mixed tissue signal, the laser data is expected to carry higher histological specificity. If a tissue section can be imaged with LD-REIMS not only are the resolution and specificity increased but also the number of data points. Most importantly, the histological analysis of consecutive sections gives proper classification data down to single cell accuracy. Thus, LD-REIMS imaging is expected to solve all problems associated with the production of training data for iKnife applications.

A proof-of-concept study was conducted where a database and a multivariate model was constructed using the imaging CO_2 setup and was validated by the iKnife instrument (**figure 6 A-B**). For laser sampling, surgical CO_2 laser was chosen as this laser allowed us to collect surgical iKnife data as well as MSI data. The combined method model showed good sensitivity (92.3%) and specificity (90.6%). Good separation was observed between healthy and cancerous tissue based on the first principal component. Cancerous laser and iKnife data points overlapped on the PCA plot; however, minor separation could be observed between laser and iKnife normal tissue spectra on the second component probably due to the improved signal-to-noise ratio with the laser. As the first component represents the highest variance, and cancerous and healthy data were separated along the PC1 axis regardless of whether it was acquired with the laser or the iKnife, the models were exchanged to test classification accuracy (**Figure 6 C-D**). Diathermy data evaluated with the laser model had 100% correct classification for normal tissue and 92% for cancerous tissue. The laser data evaluated with the diathermy model gave 97% correct classification for normal tissue and 100% for cancerous tissue. These results show that these models can be used across different ablation modalities, raising the possibility of creating

method-independent models universally applicable across all surgical energy devices and corresponding imaging modalities.

Discussion

It was demonstrated that the ion yield of atmospheric pressure desorption ionisation methods can be significantly improved by the low energy surface-induced dissociation of molecular clusters in the atmospheric interface region of the mass spectrometer. The simulation results show that if singly charged 1kDa particles with a diameter of 2.2nm are generated on the surface of a spherical collision surface positioned in the Mach disk region, the ion optics of a commercial mass spectrometer can efficiently capture these secondary ions.

Additionally, heating the impactor surface was found to yield a robust analytical setup with minimal carryover or surface fouling and further increased the overall ion yield of the desorption ionization technique. This latter effect was associated with further energy deposition into the system, facilitating the complete dissociation of supramolecular adducts. While one of the potential drawbacks of heating the impactor surface is the thermal degradation of biomolecules, as the surface reaches temperatures up to 1400K, no such effect was observed. This effect was associated with the adiabatic expansion of the gas jet after the first conductance limit, which exerts an efficient cooling effect on the transported particles, lowering the internal energy to the effective temperature range of 10-40K. Furthermore, the timeframe of the particle-surface interaction is relatively short, as individual molecules spend less than 10 μs in the vicinity of the collision surface. Thermal conductivity and thermal convection are negligible due to the vacuum environment around the impactor surface, and heat transfer through infrared radiation is insufficient to deliver enough energy in this timeframe to thermally degrade ions of interest. The described impact-based ionization enhancement setup intrinsically accelerates clusters due to the forementioned adiabatic expansion effect, resulting in a simple, robust and compact embodiment

not requiring any electrostatic field gradient. The kinetic energy of the high velocity clusters is utilized in the generation of individual molecular ions as the clusters break up resulting in a relatively low kinetic energy ion population, which is efficiently captured by a ring electrode or multipole ion guide.

The phenomena of surface – cluster interactions and the effect of it on ion formation have been less studied compared to other ion formation mechanisms. However, both electrospray ionisation and laser desorption-based methods generate clusters with sufficient kinetic energy to reach and collide with parts of the ion optics in spite of the electrostatic or pseudopotential fields utilized for ion guidance. These collisions likely result in additional uncontrolled ionization phenomena, materializing as memory effects for the user (*34*). In certain commercial atmospheric interface setups these cluster-surface collisions may significantly contribute to the observed signal.

We have implemented atmospheric interface SID in conjunction with laser desorption ionization to gain sensitivity for mass spectrometric tissue analysis. The utilization of infrared laser desorption has been an obvious choice for a method generating primarily aerosols when used for tissue ablation. While diathermal ablation involves macroscopic thermal damage including charring, UV laser desorption results in the excessive fragmentation of gaseous molecules and ions. In contrast, infrared lasers (especially short pulse width resonant mid-infrared lasers) transfer the molecular content of tissues into the gas phase efficiently and without significant thermal damage or fragmentation (*35*, *36*). These properties make the technique one of the most promising candidates for a universal tissue profiling method equally capable of tissue imaging as well as bulk or even in-vivo tissue analysis. The most serious shortcoming of LDI methods (in contrast to e.g. MALDI) has traditionally been the low ion yield, which is less critical for bulk analysis where milligrams of tissue can be ablated from tens of thousands of μm^2 area (*17*, *24*). However, histological imaging requires significantly better sensitivity, hitherto inaccessible for routine applications. The importance of universal applicability is particularly important in the

aspect of generating histologically annotated imaging data to train shallow or deep learning-driven tissue classification methods as it is described above. Furthermore, directly linking MS-guided surgery techniques with MS-based histology methods provides a unique selling point for the technique in both environments. Current histopathology tools cannot be used for real-time, interventional tissue classification or detection and similarly, current intraoperative tissue identification tools ranging from fluorescent labelling to impedance spectroscopy do not provide sufficient information for histological assessment of tissue specimens.

The presented results serve as a basis for future work regarding sample preparation-free molecular imaging of clinically important tissues and other samples. Since the technique requires no labelling, sample preparation or other user interaction with the process, the method has a high potential for non-targeted, automated molecular profiling of human disease samples.

Materials and Methods

Experimental Design:

A Waters Xevo G2-XS QToF (Waters, Wilmslow, UK) mass spectrometer was used for all experiments. The instrument was equipped with a modified REIMS source described by Balog et. al.(*31*). 100 µl/min MS grade 2–propanol (Merck, Gillingham, UK) was injected in front of the MS inlet capillary to achieve Matrix Assisted REIMS as described by Jones et. al.(*37*). A 1.5 m long, 1.6 mm I.D. PTFE tube (Merck, Gillingham, UK) was used to aspirate the aerosol from the sampling position. For the iKnife diathermy experiments, a ForceTriad (Medtronic, Watford, UK) electrosurgical generator was used in monopolar mode. The electrosurgical unit was coupled with a modified electrosurgical handpiece (Waters Research Center, Budapest, Hungary), the output power was 20W. Pork liver tissue were obtained from commercial suppliers. Ethical approval was gained from the South East London Research Ethics Committee Reference 11/LO/0686, the East of England - Cambridge East Research Ethics Committee Reference 14/EE/0024 and the project

was registered under the Imperial College Tissue Bank. Data were only obtained from patients who had consented to the use of tissue for research.

Numerical simulation:

Characterization of the flow structure was performed sequentially using different solvers and tools to cover the wide pressure range of the flow field and perform particle tracing respectively. The first step involved the application of the Reynolds-Averaged Navier-Stokes method to solve the high-pressure region inside a 70 mm, 0.5 mm I.D. inlet capillary at room temperature. A structured high-density mesh was generated to describe the laminar flow across the capillary. Zero slip velocity was imposed on the inner walls of the capillary. Mass averaged velocity, temperature and gas density values were determined at 0.2 mm from the capillary exit as 335 m/s, 240 K and 243 mbar and subsequently imposed as inlet boundary conditions for the Direct Simulation Monte Carlo (DSMC) calculations. The DSMC domain was constructed with a 5 μm cell size progressively increased to 10 μm in regions distant from the impingement target to increase computational speed without affecting the accuracy of the solution near the target. The background pressure was 3 mbar. DSMC calculations were performed in the low-pressure region of the domain using the SPARTA solver. The flow field solutions were then further processed in MATLAB and introduced into SIMION for tracing particles. A thousand 100 kDa neutral particles with 10.2 nm diameter were used to simulate solvent clusters. Their position and impact velocity were recorded and then used to generate an ion cloud of 1 kDa particles with 2.2 nm diameter.

Laser parameter characterisation and imaging

A commercially available Opolette HE2731 Optical Parametric Oscillator (Opotek, Carlsbad, USA) and a FELS25A Intelliguide CO_2 laser (Omniguide, Cambridge, USA) laser were used during the experiments. Optomechanical components were obtained from Thorlabs for the optical cage system construction (Thorlabs, Newton, USA). LA7733-E4 and LA7477-E4 ZnSe

and LA5315-E CaF_2 lenses were used for the OPO laser and only LA7733-E3 ZnSe was used for the CO_2 laser due to lack of appropriate anti-reflection coating. To test the effect of wavelength on the tissue desorption efficiency, 12 µm fresh frozen pork liver slides were sampled using the tuneable OPO laser between 2700 – 3100 nm and the laser power was normed to 5 J/cm^2. The laser energy was measured using an EnergyMax-RS J-10MB-HE Energy Sensor (Coherent, Saxonburg, USA) after the last focal lens on the defocused beam (around 10 mm from the focal spot). The fluences were calculated by measuring the area of the ablated spot sizes and the used energy for ablation using optical microscopy. The imaging experiments were done using a modified two-dimensional stage setup (Prosolia). For imaging data processing and visualization of the ion heatmap images, HDImaging (version 1.4, Waters) software was used.

Statistical Analysis:

Data processing for modelling was performed using Abstract Model Builder (AMX, version 1.1967.0, Waters). This software was used to select was used to define the spectra used for data analysis. Mass drift correction was performed against the leucine enkephalin lock mass compound (negative mode *m/z* = 554.2615), and mass binning was done to 0.1 Da. For univariate analysis, an in-house data processing pipeline was used that was written in python. Principal Component Analysis (PCA) was also performed to evaluate spectral differences using the AMX software. Principal Component Analysis (PCA) and PCA- Linear Discriminant Analysis (PCA-LDA) models were built and the PCA-LDA model was used for tissue classification. Spectral comparison for the translational study was performed with multivariate statistical approaches. Both diathermy and laser data were plotted on the same PCA-LDA model, which model was cross validated using leave – one – out cross validation method.

References and Notes

1. R. E. Honig, Laser-induced emission of electrons and positive ions from metals and semiconductors. *Appl Phys Lett*. **3**, 8–11 (1963).

2. F. J. Vastola, R. O. Mumma, A. J. Pirone, Analysis of organic salts by laser ionization. *Organic Mass Spectrometry*. **3**, 101–104 (1970).

3. F. Hillenkamp, E. Unsöld, R. Kaufmann, R. Nitsche, "Applied Physics A High-Sensitivity Laser Microprobe Mass Analyzer" (Springer-Verlag, 1975).

4. R. W. Kirschbaum, D. Prenzel, S. Frankenberger, R. R. Tykwinski, T. Drewello, Laser desorption mass spectrometry of end group-protected linear polyynes: Evidence of laser-induced cross-linking. *Journal of Physical Chemistry A*. **119**, 2861–2870 (2015).

5. G. J. Q. van der Peyl, W. J. van der Zande, P. G. Kistemaker, Kinetic energy distributions of ions produced in organic laser desorption. *Int J Mass Spectrom Ion Process*. **62**, 51–71 (1984).

6. Jean-Claude Tabet, Robert J. Cotter, Laser Desorption Time-of-Flight Mass Spectrometry of High Mass Molecules. *Anal. Chem*. **56**, 1662–1667 (1984).

7. Michael. Karas, Franz. Hillenkamp, Laser desorption ionization of proteins with molecular masses exceeding 10,000 daltons. *Anal Chem*. **60**, 2299–2301 (1988).

8. K. Dreisewerd, The Desorption Process in MALDI. *Chem Rev*. **103**, 395–426 (2003).

9. K. Wiangnon, R. Cramer, Sample Preparation: A Crucial Factor for the Analytical Performance of Rationally Designed MALDI Matrices. *Anal Chem*. **87**, 1485–1488 (2015).

10. M. Niehaus, J. Soltwisch, M. E. Belov, K. Dreisewerd, Transmission-mode MALDI-2 mass spectrometry imaging of cells and tissues at subcellular resolution. *Nat Methods*. **16**, 925–931 (2019).

11. E. A. Elia, M. Niehaus, R. T. Steven, J.-C. Wolf, J. Bunch, Atmospheric Pressure MALDI Mass Spectrometry Imaging Using In-Line Plasma Induced Postionization. *Anal Chem*. **92**, 15285–15290 (2020).

12. R. T. Steven, M. Niehaus, A. J. Taylor, A. Nasif, E. Elia, R. J. A. Goodwin, Z. Takats, J. Bunch, Atmospheric-Pressure Infrared Laser-Ablation Plasma-Postionization Mass

Spectrometry Imaging of Formalin-Fixed Paraffin-Embedded (FFPE) and Fresh-Frozen Tissue Sections with No Sample Preparation. *Anal Chem*. **94**, 9970–9974 (2022).

13. C. K. Meng, J. B. Fenn, Formation of charged clusters during electrospray ionization of organic solute species. *Organic Mass Spectrometry*. **26**, 542–549 (1991).

14. M. Gamero-Castaño, J. Fernández de la Mora, Mechanisms of electrospray ionization of singly and multiply charged salt clusters. *Anal Chim Acta*. **406**, 67–91 (2000).

15. S. A. Aksyonov, P. Williams, Impact desolvation of electrosprayed microdroplets - a new ionization method for mass spectrometry of large biomolecules. *Rapid Communications in Mass Spectrometry*. **15**, 2001–2006 (2001).

16. K.-C. Schäfer, T. Szaniszló, S. Günther, J. Balog, J. Dénes, M. Keserű, B. Dezső, M. Tóth, B. Spengler, Z. Takáts, In Situ, Real-Time Identification of Biological Tissues by Ultraviolet and Infrared Laser Desorption Ionization Mass Spectrometry. *Anal Chem*. **83**, 1632–1640 (2011).

17. N. Ogrinc, P. Saudemont, J. Balog, Y.-M. Robin, J.-P. Gimeno, Q. Pascal, D. Tierny, Z. Takats, M. Salzet, I. Fournier, Water-assisted laser desorption/ionization mass spectrometry for minimally invasive in vivo and real-time surface analysis using SpiderMass. *Nat Protoc*. **14**, 3162–3182 (2019).

18. S. Amini-Nik, D. Kraemer, M. L. C. M., K. Gunaratne, P. Nadesan, B. A. Alman, R. J. Dwayne Miller, "The Picosecond IR Laser (PIRL) Scalpel: Fundamental Limits to Minimally Invasive Surgery and Biodiagnostics" in *Imaging and Applied Optics* (OSA, Washington, D.C., 2011), p. AIWB1.

19. S. Berkenkamp, C. Menzel, M. Karas, F. Hillenkamp, Performance of Infrared Matrix-assisted Laser Desorption/Ionization Mass Spectrometry with Lasers Emitting in the 3 μm Wavelength Range. *Rapid Communications in Mass Spectrometry*. **11**, 1399–1406 (1997).

20. B. Fatou, P. Saudemont, E. Leblanc, D. Vinatier, V. Mesdag, M. Wisztorski, C. Focsa, M. Salzet, M. Ziskind, I. Fournier, In vivo Real-Time Mass Spectrometry for Guided Surgery Application. *Sci Rep*. **6**, 25919 (2016).

21. S. J. S. Cameron, Z. Bodai, B. Temelkuran, A. Perdones-Montero, F. Bolt, A. Burke, K. Alexander-Hardiman, M. Salzet, I. Fournier, M. Rebec, Z. Takáts, Utilisation of Ambient Laser Desorption Ionisation Mass Spectrometry (ALDI-MS) Improves Lipid-Based Microbial Species Level Identification. *Sci Rep*. **9**, 3006 (2019).

22. J. Balog, L. Sasi-Szabó, J. Kinross, M. R. Lewis, L. J. Muirhead, K. Veselkov, R. Mirnezami, B. Dezső, L. Damjanovich, A. Darzi, J. K. Nicholson, Z. Takáts, Intraoperative Tissue Identification Using Rapid Evaporative Ionization Mass Spectrometry. *Sci Transl Med*. **5** (2013), doi:10.1126/scitranslmed.3005623.

23. L. v. Zhigilei, B. J. Garrison, Microscopic mechanisms of laser ablation of organic solids in the thermal and stress confinement irradiation regimes. *J Appl Phys*. **88**, 1281–1298 (2000).

24. K.-C. Schäfer, J. Dénes, K. Albrecht, T. Szaniszló, J. Balog, R. Skoumal, M. Katona, M. Tóth, L. Balogh, Z. Takáts, In Vivo, In Situ Tissue Analysis Using Rapid Evaporative Ionization Mass Spectrometry. *Angewandte Chemie International Edition*. **48**, 8240–8242 (2009).

25. Y. Lu, C. L. Pieterse, W. D. Robertson, R. J. D. Miller, Soft Picosecond Infrared Laser Extraction of Highly Charged Proteins and Peptides from Bulk Liquid Water for Mass Spectrometry. *Anal Chem*. **90**, 4422–4428 (2018).

26. P. Saudemont, J. Quanico, Y.-M. Robin, A. Baud, J. Balog, B. Fatou, D. Tierny, Q. Pascal, K. Minier, M. Pottier, C. Focsa, M. Ziskind, Z. Takats, M. Salzet, I. Fournier, Real-Time Molecular Diagnosis of Tumors Using Water-Assisted Laser Desorption/Ionization Mass Spectrometry Technology. *Cancer Cell*. **34**, 840-851.e4 (2018).

27. K. Dreisewerd, R. Lemaire, G. Pohlentz, M. Salzet, M. Wisztorski, S. Berkenkamp, I. Fournier, Molecular Profiling of Native and Matrix-Coated Tissue Slices from Rat Brain by Infrared and Ultraviolet Laser Desorption/Ionization Orthogonal Time-of-Flight Mass Spectrometry. *Anal Chem*. **79**, 2463–2471 (2007).

28. A. Maimó-Barceló, J. Garate, J. Bestard-Escalas, R. Fernández, L. Berthold, D. H. Lopez, J. A. Fernández, G. Barceló-Coblijn, Confirmation of sub-cellular resolution using oversampling imaging mass spectrometry. *Anal Bioanal Chem*. **411**, 7935–7941 (2019).

29. J. C. Jurchen, S. S. Rubakhin, J. v. Sweedler, MALDI-MS imaging of features smaller than the size of the laser beam. *J Am Soc Mass Spectrom*. **16**, 1654–1659 (2005).

30. K. A. Veselkov, R. Mirnezami, N. Strittmatter, R. D. Goldin, J. Kinross, A. V. M. Speller, T. Abramov, E. A. Jones, A. Darzi, E. Holmes, J. K. Nicholson, Z. Takats, Chemo-informatic strategy for imaging mass spectrometry-based hyperspectral profiling of lipid signatures in colorectal cancer. *Proceedings of the National Academy of Sciences*. **111**, 1216–1221 (2014).

31. J. Balog, S. Kumar, J. Alexander, O. Golf, J. Huang, T. Wiggins, N. Abbassi-Ghadi, A. Enyedi, S. Kacska, J. Kinross, G. B. Hanna, J. K. Nicholson, Z. Takats, In Vivo Endoscopic Tissue Identification by Rapid Evaporative Ionization Mass Spectrometry (REIMS). *Angewandte Chemie International Edition*. **54**, 11059–11062 (2015).

32. P.-M. Vaysse, L. F. S. Kooreman, S. M. E. Engelen, B. Kremer, S. W. M. Olde Damink, R. M. A. Heeren, M. L. Smidt, T. Porta Siegel, Stromal vapors for real-time molecular guidance of breast-conserving surgery. *Sci Rep*. **10**, 20109 (2020).

33. S. E. Mason, E. Manoli, J. L. Alexander, L. Poynter, L. Ford, P. Paizs, A. Adebesin, J. S. McKenzie, F. Rosini, R. Goldin, A. Darzi, Z. Takats, J. M. Kinross, Lipidomic Profiling of Colorectal Lesions for Real-Time Tissue Recognition and Risk-Stratification Using Rapid Evaporative Ionization Mass Spectrometry. *Ann Surg*. **277**, e569–e577 (2023).

34. S. Trimpin, “Magic” Ionization Mass Spectrometry. *J Am Soc Mass Spectrom*. **27**, 4–21 (2016).

35. F. Busse, S. Kruber, W. D. Robertson, R. J. D. Miller, Digital interference microscopy and density reconstruction of picosecond infrared laser desorption at the water-air interface. *J Appl Phys*. **124**, 094701 (2018).

36. R. J. Beck, I. Bitharas, K. Ehrlich, T. I. Maisey, R. K. Mathew, A. J. Moore, J. Moor, R. R. Thomson, D. G. Jayne, J. D. Shephard, "Effects of the process dynamics in picosecond laser ablation of soft tissues" in *Optical Interactions with Tissue and Cells XXXIII; and Advanced Photonics in Urology*, H. W. Kang, R. Sroka, B. L. Ibey, N. Linz, Eds. (SPIE, 2022), p. 22.

37. E. A. Jones, D. Simon, T. Karancsi, J. Balog, S. D. Pringle, Z. Takats, Matrix Assisted Rapid Evaporative Ionization Mass Spectrometry. *Anal Chem*. **91**, 9784–9791 (2019).

Acknowledgments

We would like to thank Helen Huang from Imperial College London and Peter Kreuzaler from the Francis Crick Institute for providing mouse brain sections for experiments.

Funding: The was funded by National Institute for Health and Care Research (NIHR) Biomedical Research Centre (BRC), Waters, the Rosalind Franklin Institute, Métropole Européenne de Lille (MEL) and Cancer Research UK (CRUK) Grand Challenge programs. G. Horkovics-Kovats was supported with the professional support of the Doctoral Student Scholarship program of the co-operative doctoral program of the Hungarian Ministry of Innovation and Technology financed from the National Research, Development and Innovation fund.

Author contributions:

Conceptualization: DS, ZT, JB, JA

Investigation: DS, GH, JA, RS, HW, LL

Numerical simulations: DP

Data analysis: YX

Sample collection, histology: HH, AM

Supervision: IF, JB, ZT

Writing—original draft: DS, ZT

Writing—review & editing: DS, GH, YX, DP, JB, JB, ZT

Competing interests: The authors declare that they have no competing interests.

Data and materials availability: All data needed to evaluate the conclusions in the paper are present in the paper and/or the Supplementary Materials. All materials are available from the corresponding authors upon request.

Figures and Tables

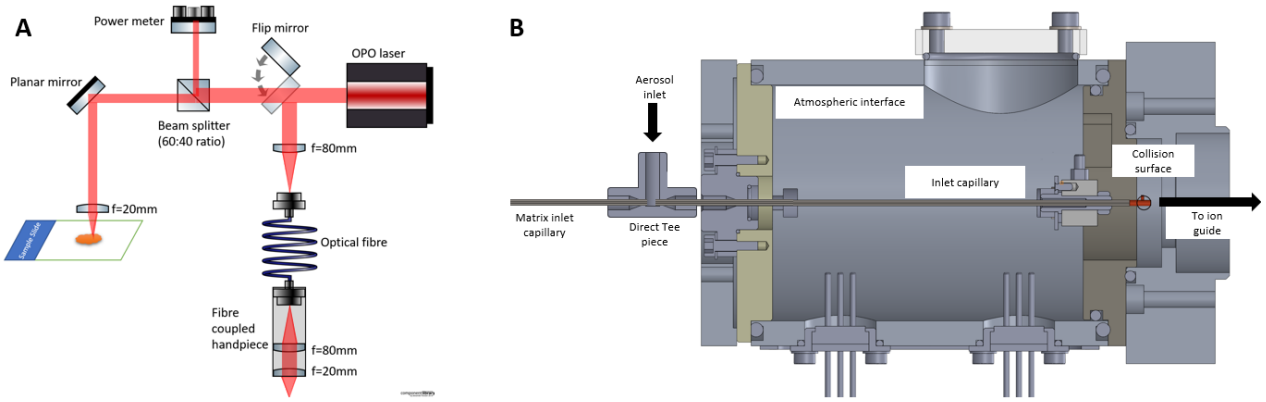

Fig. 1.: Schematics of the LD-REIMS sampling and ionisation setup.

The schematics of the prototype LD-REIMS imaging platform can be seen on figure A. The laser source (in this case the OPO laser) is emitting the beam, which can be directed using a flip mirror towards an optical fibre-coupled handpiece that allows the free analysis of bulk tissue samples without the spatial information. The second option if the mirror is not used is the high-resolution imaging setup, where the beam is first split with a power meter (for continuous power monitoring) then directed and focused onto the glass slide holding the sample, which is positioned on a 2D XY motorized stage. The generated aerosol is evacuated and introduced to the atmospheric interface (B) through the Direct Tee piece. A continuous matrix solvent is added

through the matrix inlet capillary, and the droplet-fused aerosols enter the vacuum through the inlet capillary. After exiting the inlet capillary, the droplets go through an acceleration via the carrier gas' adiabatic expansion, and hit the high temperature collision surface, where free gas phase ions are liberated from the aerosol droplets, which can be collected by the ion guide and analyzed by the mass spectrometer downstream.

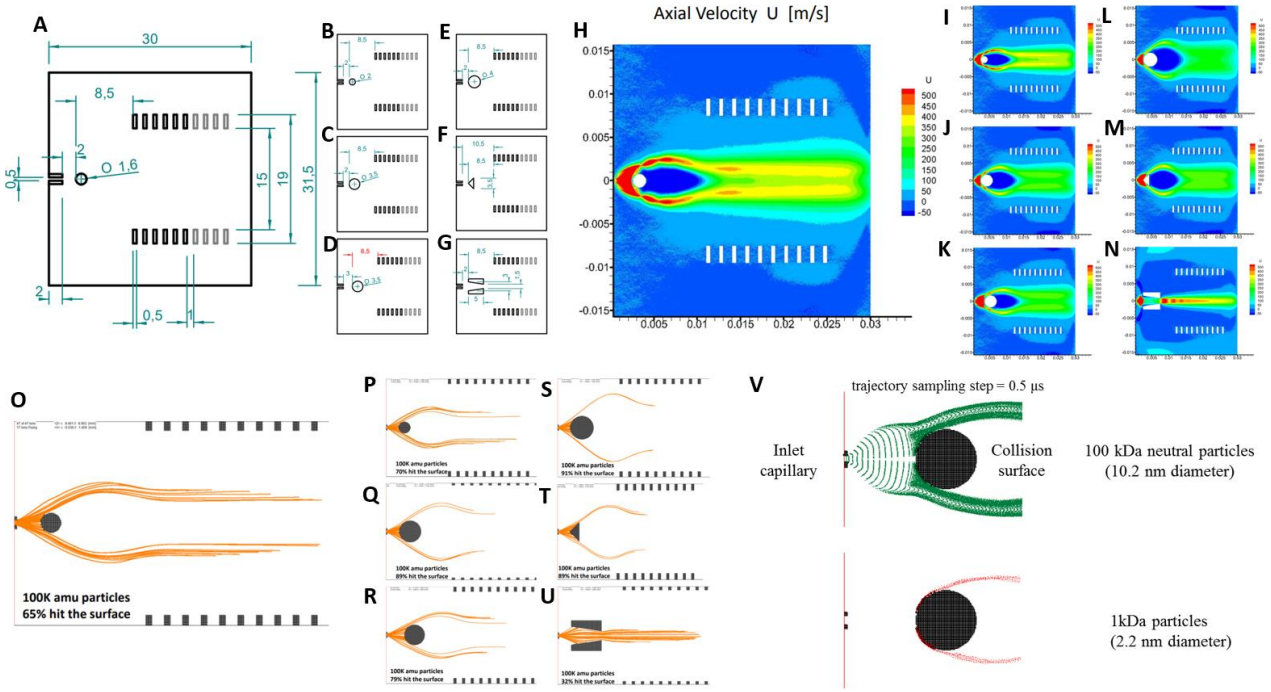

Fig. 2.: Optimisation of the impactor surface using DSMC numerical simulations.

The prototype atmospheric interface design allowed the rapid and efficient experimental characterisation of different collision surface geometries in addition to the numerical simulation data. DSMC simulations were performed in the modelled atmospheric interface environment using the following geometries: 1.6 mm sphere, 2 mm distance from inlet capillary (A), 2 mm sphere, 2 mm distance from the inlet (B), 3.5 mm sphere, 2 mm from inlet (C), 3.5 mm sphere, 3 mm from inlet capillary (D), 4 mm sphere, 2 mm from the inlet (E), 3.5 mm cone, 2 mm from inlet capillary (F), 3-1.5 mm decreasing funnel, 5 mm long, 2 mm from inlet capillary (G). The axial velocity profiles (H-N) were characterised, and 100k amu particle collision simulations (O-U) were performed. Simulation results for the interaction of particles with a spherical collision

surface, derived from DMSC calculations followed by particle tracing were also conducted (V).

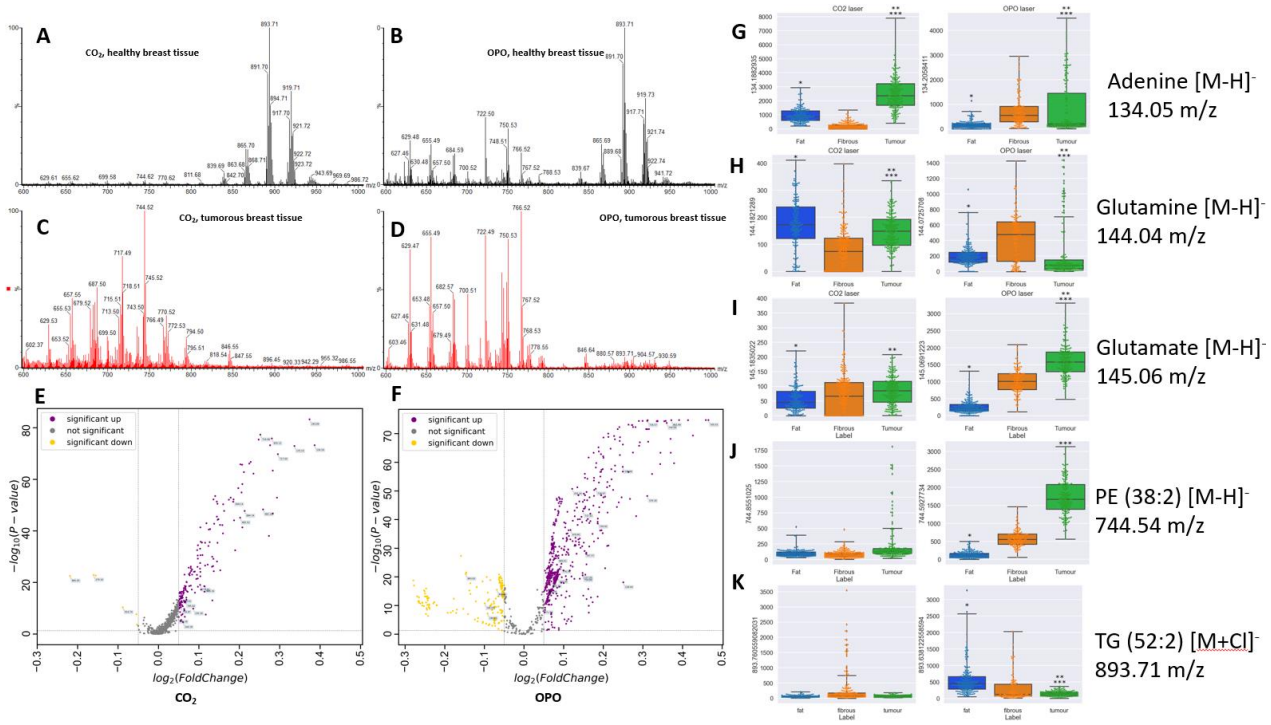

Fig. 3.: Lipidomic and metabolomic characterisation of breast cancer samples using LD-REIMS.

Ex vivo human breast samples were analysed using two different IR lasers (OPO and CO_2) using the LD-REIMS method. The tissues contained healthy and cancerous sections, validated by histopathology analysis. The spectra observed in the lipid region (m/z 600 – 1000) show characteristic differences of elevated levels of triglycerides in the healthy breast tissue (A-B) and phospholipids are more prevalent in the tumorous samples (C-D). Volcano plots generated from the data obtained with the two lasers (E-F) allow us to identify numerous metabolites and phospholipids that show statistically significant fold changes. Univariate plots of identified molecules of Adenine $[M-H]^-$ (G), Glutamine [M-H]- (H), Glutamate $[M-H]^-$ (I), Phosphatidylethanolamine PE(38:2) $[M-H]^-$ (J) and Triglyceride TG(52:2) $[M+Cl]^-$ (K) show significant differences between different tissue types. * Statistically significant difference between fat and fibrous tissue ** Statistically significant difference between tumour and fat tissue *** Statistically significant difference between tumour and fibrous tissue.

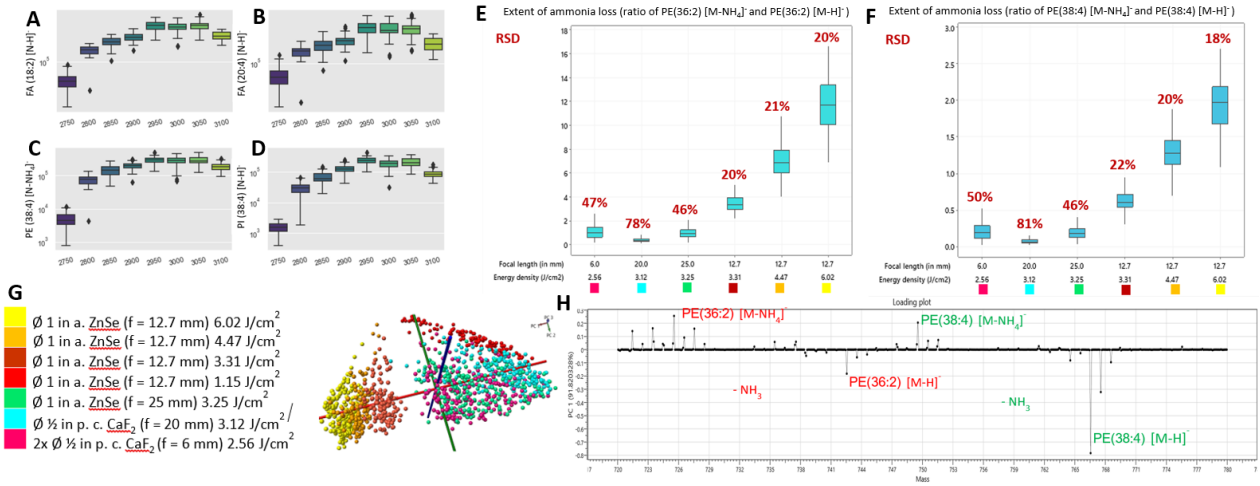

Fig. 4.: Effects of laser fluence on the spectral composition and molecule fragmentation.

The tunable OPO laser allowed the characterisation of the effect of wavelength on the desorption process on pork liver tissue. The available wavelength range (2700 – 3100 nm) was scanned in 50nm resolution; the laser energy was normed to the same fluence. Spectral profiles were recorded in the range of 2750 – 3100, 2700 nm provided no observable spectra due to low laser absorption rates. The intensity profile of four known molecules over the tested range (FA 18:1, FA 20:4, PE 38:4 and PI 38:4) (A-D) show an optimal desorption wavelength at around 2900 – 3000 nm. This falls in line with the water absorption maxima observed at 2940 nm in the mid-IR range originating from the O – H bond stretch absorption. The loss of ammonia from phosphatidylethanolamine lipids can be observed with the LD REIMS process. The ratio of observed ions of two PE species (PE(36:2) and PE(38:4)) originating from pork liver samples is shown to increase as the laser fluence increases (E-F). The PCA model can distinguish between spectra acquired at different fluence levels, as seen in plots G and H. The deamination process of PE species becomes prevalent with laser fluence levels above 3.3 J/cm^2.

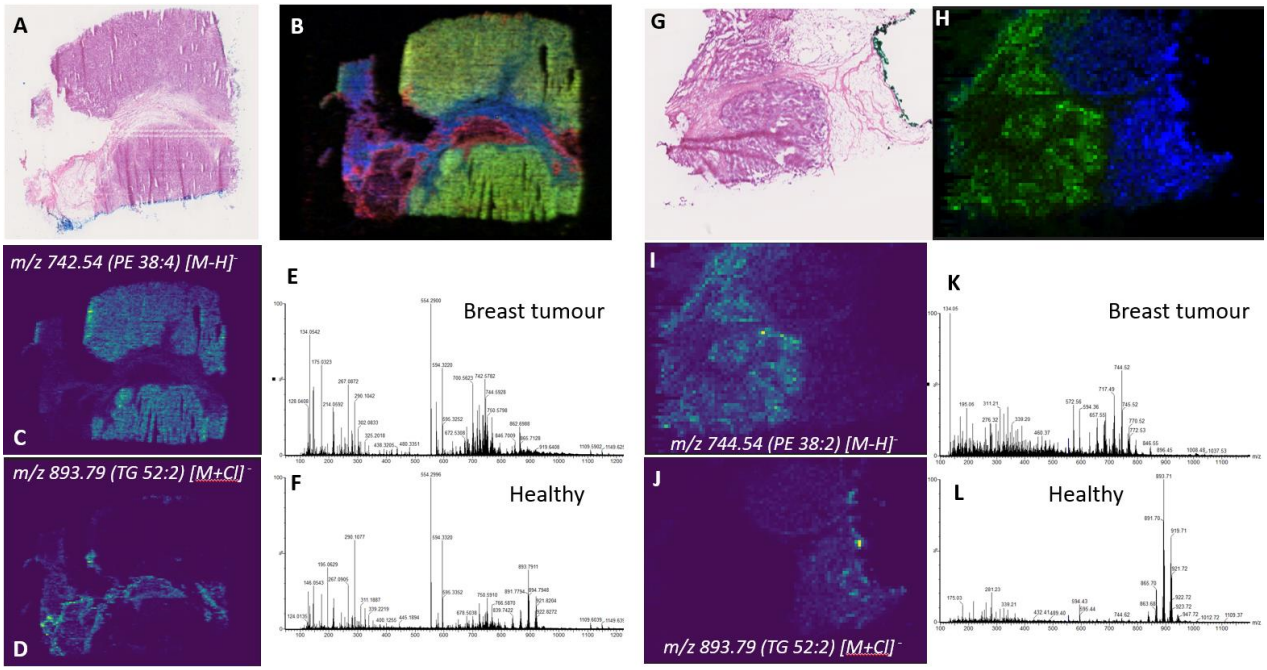

644

645 **Fig. 5.: Biological imaging study of two breast cancer samples using OPO and CO_2 lasers.**
646 The breast cancer samples were analysed using the two lasers at 70 um raster sizes. Consecutive
647 tissue sections were H&E stained and classified by pathologists (A and G). The results of the
648 OPO imaging can be seen in figure B-E, where the composite RBG image (B) is visualised (Red:
649 893.79 m/z (TG 52:2 $[M+Cl]^-$), Green: 742.54 m/z (PE 38:4 $[M-H]^-$), Blue: 281.23 m/z (FA18:1
650 $[M-H]^-$)). The results of the CO_2 laser can be seen in figures G-K, where the composite image (H)
651 is visualised (Blue: 893.79 m/z (TG 52:2 $[M+Cl]^-$), Green: 742.54 m/z (PE 38:2 $[M-H]^-$)).
652 Individual ion images for different ionic species (C-D for OPO and I-J for CO_2) show good
653 differentiation between different histological status tissues, and the 50 – 1200 m/z spectra of
654 different annotated regions (E-F for OPO and K-L for CO_2) show clear differences between the
655 metabolic and lipidomic fingerprint of healthy and cancerous tissues.

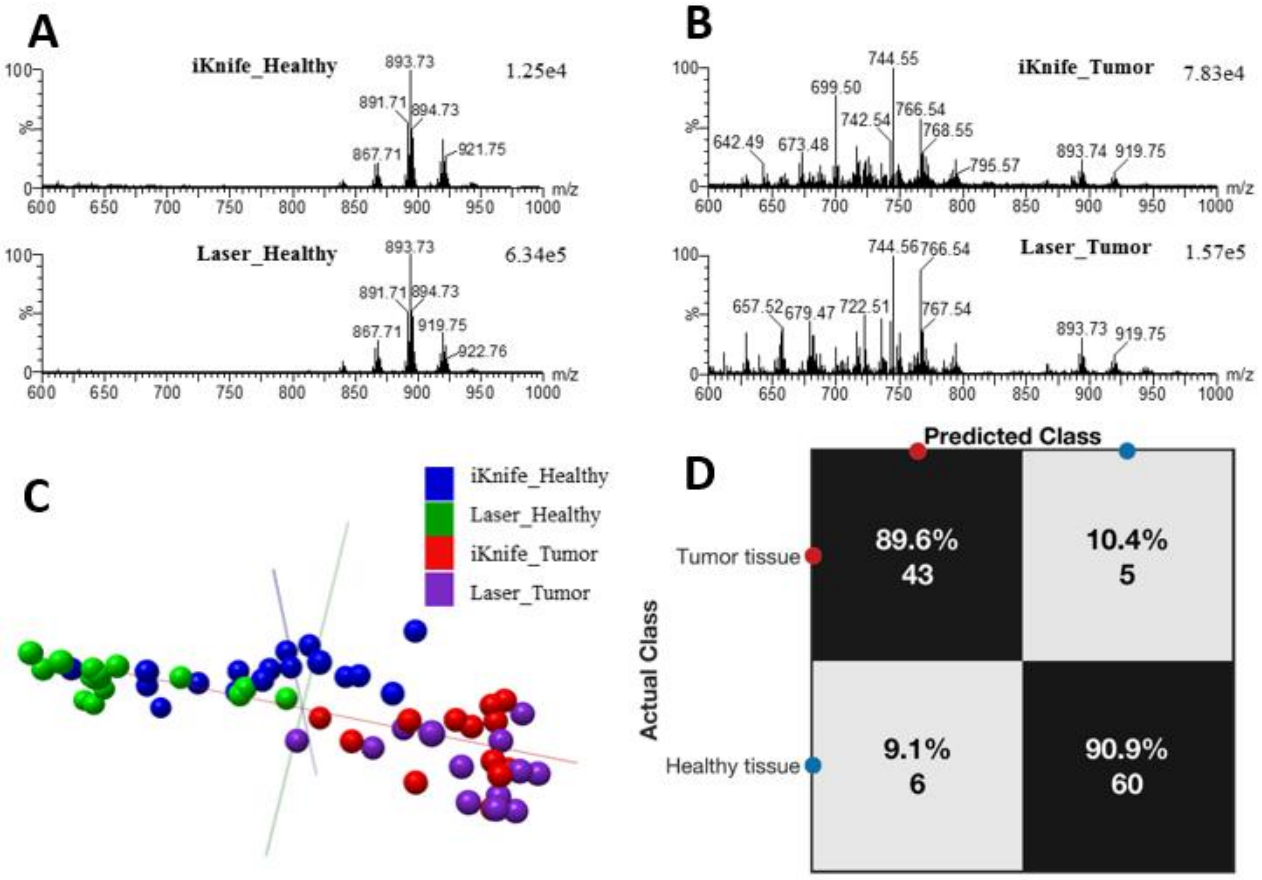

Fig. 6.: **Translational capabilities between intraoperative iKnife technique and digital pathology LD-REIMS experiments.**

Spectral comparison between different breast tissue types obtained with the laser and iKnife methods was performed using breast cancer samples (A-B). A PCA model was built from the obtained data for tissue classification (B). Leave-one-out cross-validation was performed from the previously built PCA-LDA model; the model yielded good sensitivity (92.3%) and specificity (90.6%) (C-D).